

PCCP

Accepted Manuscript



This is an *Accepted Manuscript*, which has been through the Royal Society of Chemistry peer review process and has been accepted for publication.

Accepted Manuscripts are published online shortly after acceptance, before technical editing, formatting and proof reading. Using this free service, authors can make their results available to the community, in citable form, before we publish the edited article. We will replace this *Accepted Manuscript* with the edited and formatted *Advance Article* as soon as it is available.

You can find more information about *Accepted Manuscripts* in the [Information for Authors](#).

Please note that technical editing may introduce minor changes to the text and/or graphics, which may alter content. The journal's standard [Terms & Conditions](#) and the [Ethical guidelines](#) still apply. In no event shall the Royal Society of Chemistry be held responsible for any errors or omissions in this *Accepted Manuscript* or any consequences arising from the use of any information it contains.

Revealing chemical ordering in Pt-Co nanoparticles using electronic structure calculations and X-ray photoelectron spectroscopy

Gábor Kovács,^a Sergey M. Kozlov,^a Iva Matolínová,^b Mykhailo Vorokhta,^b Vladimír Matolín,^b
Konstantin M. Neyman^{*a,c}

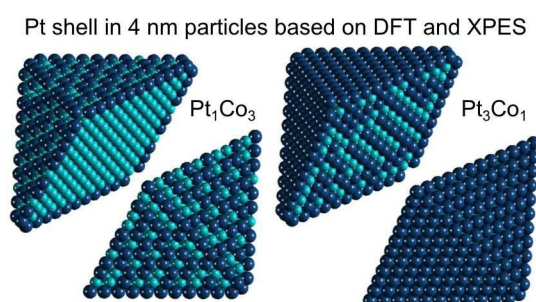
^a *Departament de Química Física and Institut de Química Teòrica i Computacional (IQTCUB),
Universitat de Barcelona, c/ Martí i Franquès 1, 08028 Barcelona, Spain*

^b *Department of Surface and Plasma Science, Charles University, V Holešovičkách 2, 18000 Prague,
Czech Republic*

^c *Institució Catalana de Recerca i Estudis Avançats (ICREA), 08010 Barcelona, Spain
E-mail: konstantin.neyman@icrea.cat*

Abstract. High catalytic activity of Pt-Co nanoalloys in the oxygen reduction and other reactions is usually attributed to their Pt-rich surfaces. However, identification of the precise near-surface structure is by no means easily achievable experimentally. In this work we systematically analyzed the chemical ordering and surface composition of $\text{Pt}_x\text{Co}_{79-x}$ and $\text{Pt}_x\text{Co}_{140-x}$ bimetallic nanoparticles by means of a recently developed method based on topological energy expressions and electronic structure calculations. Pt is found to segregate on the surface, especially on corner and edge sites, forming a one atomic layer thick skin independently of the size and composition of the nanoparticle. In turn, the subsurface shell of the particle is composed mostly of Co, whereas the core area has a mixed composition, which depends on the overall stoichiometry. The formation of an outer Pt shell is corroborated by thoroughly analyzed data of X-ray photoelectron spectroscopy experiments performed with various photon energies on annealed Pt-Co particles prepared in vacuum by magnetron sputtering. The core-shell structure of Pt-Co particles is calculated to be more stable than the respective L1_0 structure. The obtained topological energy expressions are shown to depend only very moderately on the nanoparticle size, which allowed us to apply them to determine the ordering in ~ 4 nm big $\text{Pt}_x\text{Co}_{1463-x}$ species. The presented results deepen our understanding of the intrinsic structure of Pt-Co nanoparticles depending on their size and composition.

TOC image:



TOC text:

$\text{Pt}_\gamma\text{Co}_{1-\gamma}$ -core@Co-rich-subsurface@Pt-shell structure is identified in several nm large Pt-Co particles using X-ray photoelectron spectroscopy and an optimization method based on density-functional calculations.

Introduction

Nanoalloys based on platinum have attracted much attention of researchers for the last decades due to several important reasons. First, some of these materials have singular magnetic properties, e.g. magnetic anisotropy above the “super-paramagnetic limit”, which render them interesting for high-density information storage and electromagnetic devices.¹⁻⁵ Another reason is that Pt-based nanoalloys can be remarkably active catalysts despite the lowered Pt-content and consequently reduced cost.⁶ This high activity is usually rationalized by preferential occupation of surface sites by Pt.⁷ For instance, Pt-Co nanoalloys are highly efficient catalysts in Fischer-Tropsch synthetic reactions and in low-temperature fuel cells, amongst other applications.⁸⁻¹¹ Recently we have shown that magnetron-sputtered Pt-Co catalysts are very efficient (per gram of Pt) for the oxygen reduction reaction.¹²

For a deeper comprehension of the catalytic behavior of (magnetron-sputtered) Pt-Co nanoalloys, the first step is the understanding of the structure of nanoparticles (NPs) of different sizes and compositions present in the catalysts. The size and composition are often defined by the preparation conditions. However, alloy NPs with a given size, composition and shape have an additional degree of freedom, chemical ordering. The latter is the pattern, in which atoms of two metals occupy structural positions imposed by the NP lattice. Naturally, more thermodynamically stable patterns are easier to obtain experimentally. In spite of the recent progress in experimental structural analysis, such as advances in electron microscopy techniques, it is still hardly feasible to precisely determine the three-dimensional chemical ordering in a bimetallic NP based solely on experimental data.

As far as the most pertinent experimental works on the structural analysis of Pt-Co NPs are concerned, it was found that PtCo forms an ordered L1₀ crystalline phase at the equiatomic composition.¹³⁻¹⁵ The transition from disordered A1 phase to ordered L1₀ phase was observed upon annealing during the synthesis of the NPs.¹⁴ However, several experimental studies identified Co core – Pt shell or Pt-Co core – Pt shell NPs.^{11,16} Mayrhofer et al. found that segregation in Pt-Co nanocatalysts induced by CO adsorption led to the formation of a Pt-shell around a Pt-Co core. The resulting catalyst particles featured high activity despite the low Pt content.¹⁷ Recently Xin et al.¹⁸ used pumped gas cell transmission electron microscopy (TEM) observations to describe the surface segregation of Co in Pt-Co NPs in oxidizing environments.

Computational search for the lowest-energy geometric structure and the lowest-energy chemical ordering of a fixed geometric shape, which is referred to in the literature as global optimization problem,^{19,20} has still been an uphill task for particles of several nm in size. Several theoretical studies were dedicated to assess the structure of different sized Pt-Co NPs. For instance, Chui et al.²¹ studied the structures and atomic distributions of Pt-Co NPs of 500 atoms by classical molecular dynamic simulations using interatomic potentials. There, structures of Co-core – Pt-shell NPs of different Pt:Co atomic ratios were optimized using a thermal annealing technique. It was found that Pt preferred to attain both surface and near-surface positions independently of the Pt:Co ratio. Mottet et al. have carried out global-optimization and Monte-Carlo studies with interatomic potentials²² in order to investigate the structure of Pt-Co particles within the 1-3 nm size range. They found that structural and chemical ordering depends on the NP size. For NPs of less than 100 atoms, the most stable are polyicosahedral-like species, whereas for NPs of more than 100 atoms the most favorable structures are decahedral with a pseudo-L1₀ phase ordering in all the tetrahedral units with alternating pure pentagonal ring layers along the fivefold symmetry axis. The same computational strategy has been applied to describe order ↔ disorder transitions in 800-atom Pt-Co NPs.²³ The size dependence of the shape of Pt-Co NPs has also been supported by experimental results.²⁴⁻²⁶ Qin et al.²⁷ analyzed Pt-Co NPs

of different sizes, shapes and compositions by means of Monte-Carlo simulations and showed that Co atoms prefer to occupy bulk positions, whereas Pt tends to segregate on the surface.

Recently Baletto et al.²⁸ used one-by-one atom deposition based on classical molecular dynamics method combined with density-functional theory (DFT) calculations to explore new structural motifs in Pt-Co nanoalloys composed of 55 - 155 atoms. A novel structural motif of two stacked poly-icosahedral pancakes has been shown to have unexpectedly high stability. Monte-Carlo simulations by Chepulskii et al.²⁹ based on local cluster expansions for bulk alloys predicted strong Pt segregation in the first (surface) layer and Co segregation in the second (subsurface) layer with the formation of a core/Co/Pt or “onion shell” profile. The structure of the core varied between $L1_0$ and random alloy depending on the simulation temperature. In most of the aforementioned studies interatomic potentials were employed to generate structures by molecular dynamics simulations, whereas Hu et al.³⁰ investigated the electronic and magnetic properties of manually selected Pt_xCo_{N-x} ($N \leq 55$) NP structures by means of DFT calculations and found that Pt atoms tend to occupy surface sites forming an exterior shell. Noh et al. also applied DFT calculations to approximately 430 systematically selected Pt-Co NPs of different sizes and compositions. They concluded that the most thermodynamically stable NPs have onion structure, in which the outermost shell consists of Pt.³¹

As follows from the overview of the literature, both experimental and theoretical studies show a rather mixed picture about the most stable chemical ordering in Pt-Co nanoalloys. In particular, computational studies are limited either by the degree of accuracy of classical molecular dynamics and interatomic potentials or by the computational cost of extensive DFT screening of NP structures. We have recently proposed a methodological framework that provides an efficient way for the optimization of chemical ordering in bimetallic NPs with almost DFT accuracy.³² The new approach is based on the concept of the topological energy expression, E_{TOP} (see the Methodology section for more details), which accounts for a set of important structural features that determine the relative stability of bimetallic NPs of a particular size and shape. These features include 1) energy gain/loss due to heteroatomic bond formation, 2) distinct coordination numbers of atoms in different sites of the NP, and 3) possible tetragonal distortion in $L1_0$ alloys. In the topological energy expression, one energetic value (referred to as *descriptor*) corresponds to each of the aforementioned structural features, which makes the interpretation of our results particularly straightforward.

Herein, we present a joint computational and experimental study of the near-surface chemical ordering in Pt-Co NPs. We carried out a comprehensive computational structural analysis for both the Pt_xCo_{79-x} ($19 \leq X \leq 60$) and Pt_xCo_{140-x} ($X = 96, 105$) NPs of truncated octahedral *fcc* structure. To obtain a deeper understanding of Pt-Co alloying at nanoscale we determined topological energy expressions for various NPs. Descriptors obtained for Pt-Co NPs are found to depend mostly on the composition of the NP, and much less on its size. This finding provided firm grounds for the optimization of chemical ordering in much larger NPs, such as Pt_xCo_{1463-x} ($366 \leq X \leq 1097$) also investigated in this work. Based on our results we predict Pt_yCo_{1-y} -core@Co-rich-subsurface@Pt-shell structures to be the most thermodynamically stable. Formation of such structures is confirmed by our X-ray photoelectron spectroscopy (XPES) experiments performed with photon energies of 180, 650 and 5950 eV on annealed sputtered Pt-Co films. We also analyzed the electronic structure (*d*-band center) and average interatomic distances in the NPs as a function of the Pt:Co ratio. These results allowed us to characterize chemical ordering in Pt-Co NPs covering a broad range of sizes and compositions.

Methodology

Our methodology for the optimization of chemical ordering in nanoalloys with different compositions³² is summarized in the following. The energy of a given $\text{Pt}_x\text{Co}_{N-x}$ NP is approximated by the topological energy E_{TOP} defined by expression (1) that depends only on the mutual positions of X Pt and (N-X) Co atoms in a predetermined lattice:

$$E_{TOP} = E_0 + \varepsilon_{BOND}^{Pt-Co} N_{BOND}^{Pt-Co} + \varepsilon_{CORNER}^{Pt} N_{CORNER}^{Pt} + \varepsilon_{EDGE}^{Pt} N_{EDGE}^{Pt} + \varepsilon_{TERRACE}^{Pt} N_{TERRACE}^{Pt} \quad (1)$$

where N_{BOND}^{Pt-Co} is the number of heteroatomic bonds (nearest-neighbor Pt-Co pairs of atoms) in the considered structure; N_{CORNER}^{Pt} , N_{EDGE}^{Pt} , and $N_{TERRACE}^{Pt}$ are the numbers of Pt atoms on corners, edges and terraces, respectively; E_0 is a constant (for each studied NP composition $\text{Pt}_x\text{Co}_{N-x}$) minimizing the offset of the total energies of homotops calculated by the chosen electronic structure method versus the corresponding E_{TOP} values from eq. (1).

To every characteristic number N_i in eq. (1) corresponds an energetic factor ε_i , called descriptor. Very importantly, each of these four descriptors has a well-defined physical meaning. $\varepsilon_{BOND}^{Pt-Co}$, for instance, represents the energy gain as a result of mixing Pt with Co (per formed Pt-Co bond). The other descriptors $\varepsilon_{CORNER}^{Pt}$, ε_{EDGE}^{Pt} and $\varepsilon_{TERRACE}^{Pt}$ reflect the energy gain or loss resulting from the exchange of a Pt atom on a corner, an edge or a terrace with a Co atom in the NP interior (given that the number of heteroatomic bonds N_{BOND}^{Pt-Co} remains constant). Therefore, the energy expression E_{TOP} can be tailored for every NP structure with a given shape, size and composition through fitting the ε_i descriptors to the total energies E_{ES} of appropriate electronic structure (ES, e.g. DFT) calculations of several isomers (homotops) via multiple linear regression.³³ Note that the constant E_0 appears as the intercept in the multiple linear regression procedure. For simplicity, when we discuss contributions of $\varepsilon_i N_i$ terms to the energy of the global minimum, we refer to the $E_{TOP} - E_0$ value.

Calculations of electronic structure total energies E_{ES} for various NPs are the bottleneck of the method, since they are time consuming for larger NPs. (Note, however, that calculations of a limited number of bimetallic NPs composed of 140 atoms were affordable already in 2004³⁴ and in the meantime notably larger NPs became accessible for the DFT supercomputing.³⁵⁻³⁷) On the other hand, insufficient number of structures in the fitting set leads to poor statistical accuracy of the obtained ε_i values. The accuracy of the individual descriptors ε_i can be estimated as 95% confidence intervals via the bootstrap method.³⁸ The overall precision δ of the energies E_{TOP} is estimated as twice the residual standard deviation (RSD) between E_{ES} and E_{TOP} energies for a set of $N_{TEST} \geq 10$ structures *not* included in the fitting procedure

$$\delta = 2 \sqrt{\frac{\sum(E_{ES} - E_{TOP})^2 - (\sum(E_{ES} - E_{TOP}))^2}{N_{TEST} - 1}} \quad (2).$$

The accuracy (ΔE) of the expression (1) can be estimated by the energy difference between the lowest-energy structure according to ES calculations and the global minimum structure according to the topological energy expression. The energy difference between these two structures can be calculated both as ΔE_{TOP} (the energy difference between the two homotops using the energies given by the topological expression) and ΔE_{ES} (the energy difference between the two homotops using DFT energies). Since different structures with the same N_i numbers by definition yield the same E_{TOP} , but can have slightly different E_{ES} due to minor effects not accounted for in the topologic energy expression, it is more consistent to calculate the accuracy (ΔE) as ΔE_{TOP} using values obtained from eq. (1).

A topological energy expression constructed for a given system can be used for the optimization of its chemical ordering within a predetermined lattice. Monte-Carlo simulations are carried out in steps of simultaneous exchanges of n random atoms of Pt with n random Co atoms. The number of atoms to be exchanged is selected in a random way with the probability $p(n) \sim n^{-3/2}$. It was shown that even very significant barriers in the configurational space can be overcome using these moves.³²

The temperature during a Monte-Carlo simulation is chosen in such a way that the system spends <50 % of the time in the lowest-energy configuration. For a particular $\text{Pt}_x\text{Co}_{N-x}$ NP a configuration was considered to be global minimum, if a move from it to a lower energy structure failed after $10 * X(N - X)$ multiple exchange moves.

During the Monte-Carlo simulations, when the program finds a structure with lower energy than the previously calculated ones, the geometry is written into a file. N_{TEST} structures featuring the lowest E_{TOP} energies were calculated by the chosen ES technique described in the next section. The resulting set of E_{ES} energies is used to estimate the precision δ of the E_{TOP} employed in the Monte-Carlo simulation. If the resulting δ was above 200 meV, the test set of structures was added to the fitting set and new descriptors were determined. Then global optimization with the new energy expression led to a new test set generated in the aforementioned way, and the precision δ of this new E_{TOP} was estimated on these new structures, which had not been included in the fitting.

Computational details

Electronic structure calculations have been performed using the periodic plane-wave code VASP.³⁹ The employed gradient-corrected exchange-correlation functional PBE⁴⁰ was found to be one of the most appropriate among common functionals for the description of transition metals.^{41,42} The projector augmented wave approach was applied to treat the interaction between valence and core electrons.⁴³ We carried out calculations with plane wave basis sets defined by 268.0 eV energy cut-off. Our benchmarks for Pd-X NPs have shown a negligible effect of the cut-off energy increase to 415.0 eV on all chemical ordering optimization results.³² The one-electron Kohn-Sham states were smeared by 0.1 eV using the first-order method of Methfessel and Paxton;⁴⁴ finally, converged energies were extrapolated to the zero smearing. All calculations were performed at the Γ -point in the reciprocal space only. The relaxation of all atoms was carried out during the geometry optimization until forces on each of them became < 0.2 eV/nm. The minimal separation between NPs in adjacent supercells exceeded 0.7 nm, at which the NP-NP interaction was found to be negligible.^{35,45} Since cobalt is a magnetic element, spin polarized calculations have been carried out throughout.

Experimental details

The PtCo catalyst films with a thickness equivalent to 10 nm have been prepared by simultaneous DC magnetron sputtering of Pt and Co. The deposition has been carried out in Ar atmosphere of a total pressure of 6×10^{-1} Pa at 20 W power applied to both the Co and Pt targets giving a growth rate of the PtCo film of $3.3 \text{ nm} \cdot \text{min}^{-1}$. The soft X-ray photoelectron spectroscopy (SXPS) study was performed at the Materials Science Beamline, Elettra synchrotron light facility in Trieste, Italy. The bending magnet source provides synchrotron light in the energy range of 21-1000 eV. Hard X-ray photoelectron spectroscopy (HAXPES) measurements were performed at the BL15XU beamline of the SPring-8 synchrotron facility in Japan. The X-ray was monochromatized at 5950.2 eV by using a Si (333) channel-cut post-monochromator. The total energy resolution $\Delta E = 280 \text{ meV}$ was determined from the Fermi edge of an Au reference sample. All the SXPS and HAXPES experiments were performed ex situ in ultrahigh vacuum (UHV) experimental chambers operating at base pressures around 5×10^{-9} mbar, and the spectra were taken at the grazing photon incidence and normal emission geometry. The PtCo film

morphology observations were performed by means of Atomic Force Microscopy (AFM) and Transmission Electron Microscopy (TEM) using a Bruker Multimode 8 microscope and a 200kV JEOL 2100F microscope, respectively.

Results and discussion

We carried out calculations as outlined above to analyze the chemical ordering in $\text{Pt}_x\text{Co}_{79-x}$ and $\text{Pt}_x\text{Co}_{140-x}$ NPs of truncated octahedral *fcc* structure, which is in line with the Wulff construction at the considered NP sizes. However, we also showed that the factors governing the chemical ordering (the actual descriptor values) do not change much for different shapes.³² We investigated $\text{Pt}_x\text{Co}_{79-x}$ NPs of different compositions ($19 \leq X \leq 60$) and also performed calculations for $\text{Pt}_x\text{Co}_{140-x}$ ($X = 96, 105$) particles to assess the transferability of descriptor values between NPs of different size. For all considered NPs the precision, δ , of topologic energy expressions was found to be better than 200 meV (i.e. better than 2 meV per atom). That is, topologic energy expressions were found to describe sufficiently accurately alloys composed of metals with notably different atomic sizes. (Bulk-optimized interatomic distances in bulk Pt and Co are 281 and 247 pm, respectively.⁴¹) Finally, on the basis of the results showing that the particle size has a quite limited effect on the actual descriptor values, we predicted the chemical ordering in notably larger $\text{Pt}_x\text{Co}_{1463-x}$ ($366 \leq X \leq 1097$) NPs of ca. 4 nm, which are too big for DFT calculations. We showed that the formation of Pt skin in medium-sized Pt-Co nanoparticles may be hindered by Pt accumulation in the NP core. For instance, the 100% perfect Pt skin does not form in Pt_1Co_1 NPs smaller than 5 nm, because the core composition stays around Pt_1Co_2 in this size range.

Results for $\text{Pt}_x\text{Co}_{79-x}$ nanoparticles

Four different compositions of $\text{Pt}_x\text{Co}_{79-x}$ NPs have been analyzed that correspond to approximately 1:3, 1:1, 2.2:1 and 3:1 Pt:Co ratios. These compositions are typically used in catalytic experiments and with these compositions we covered the spectrum of Pt-rich, Co-rich and equiatomic compositions.

Table 1. Descriptors (ε_i) in the topologic energy expressions for $\text{Pt}_x\text{Co}_{79-x}$ and $\text{Pt}_x\text{Co}_{140-x}$ nanoparticles as well as the corresponding precision (δ) and accuracy (ΔE) values (all in meV). 95% confidence intervals of ε_i are also given, e.g. -67_{-29}^{+33} means that the interval is $-96 \div -34$ meV. N_{FIT} is number of structures used to perform the fitting of the descriptors.

| | $\text{Pt}_{19}\text{Co}_{60}$ | $\text{Pt}_{40}\text{Co}_{39}$ | $\text{Pt}_{54}\text{Co}_{25}$ | $\text{Pt}_{60}\text{Co}_{19}$ | $\text{Pt}_{96}\text{Co}_{44}$ | $\text{Pt}_{105}\text{Co}_{35}$ |
|------------------------------|--------------------------------|--------------------------------|--------------------------------|--------------------------------|--------------------------------|---------------------------------|
| $\varepsilon_{BOND}^{Pt-Co}$ | -67_{-29}^{+33} | -30_{-6}^{+9} | -25_{-14}^{+10} | -35_{-9}^{+10} | -51_{-6}^{+9} | -45_{-11}^{+8} |
| $\varepsilon_{CORNER}^{Pt}$ | -1309_{-181}^{+107} | -436_{-106}^{+99} | -523_{-142}^{+94} | -596_{-60}^{+62} | -587_{-54}^{+53} | -667_{-116}^{+94} |
| ε_{EDGE}^{Pt} | -1230_{-204}^{+108} | -884_{-196}^{+153} | -720_{-97}^{+118} | -714_{-103}^{+130} | -680_{-103}^{+68} | -733_{-97}^{+88} |
| $\varepsilon_{TERRACE}^{Pt}$ | -918_{-139}^{+104} | -327_{-85}^{+81} | -415_{-126}^{+117} | -525_{-34}^{+23} | -504_{-35}^{+29} | -464_{-36}^{+57} |
| N_{FIT} | 23 | 46 | 35 | 52 | 21 | 35 |
| precision, δ | 118 | 150 | 187 | 154 | 137 | 155 |
| accuracy, ΔE | 48 | 89 | 68 | 95 | 116 | 74 |

$\text{Pt}_{19}\text{Co}_{60}$. We carried out the analysis of the descriptor contributions for a Co-rich NP of 79 atoms, in which the ratio Pt:Co is 1:3. The results showed that Pt atoms tend to segregate on the surface (Figure 1). The energy gain corresponding to the occupation of 6-coordinated corner and 7-coordinated edge positions by Pt is rather similar (1309 and 1230 meV, respectively), whereas the energy gain for terrace positions is smaller, 918 meV (Table 1). When we analyze the structure of the global minimum $\text{Pt}_{19}\text{Co}_{60}$ NP, we note that both the subsurface and the core parts consist of pure cobalt, whereas all Pt atoms are located in low-coordinated surface positions (Figure 1, Table 2). These Pt atoms occupy only edge and

corner positions, while terraces are fully composed of Co. The calculated energy contributions to the global minimum for corner and edge positions of Pt atoms are 49% and 24%, respectively (Figure 2). Since no Pt atoms are found in terrace position in the global minimum structure, there is no energy gain from that channel. The energy of heteroatomic bonds was calculated to be 67 meV. Although this value seems rather small, as the number of heteroatomic bonds is high (115 in this case), the overall contribution of Pt-Co bonds to the energy is quite substantial (around 25%).

Pt₄₀Co₃₉. For the Pt-Co NPs of approximately 1:1 composition segregation of Pt on the surface of NPs was found to be favorable, and the corresponding energy gains were 884 meV for each Pt atom on 7-coordinated edge positions, 436 meV for Pt on 6-coordinated corners and 327 meV for 9-coordinated terrace positions (Table 1). The respective contributions to the energy of the global minimum of the NP are 43%, 33%, and 10% (Figure 2). The contribution of each of 116 heteroatomic bonds to E_{TOP} is 30 meV, which gives 14% contribution to the overall energy gain. Note that the calculated value of $\varepsilon_{BOND}^{Pt-Co} = -30_{-6}^{+9}$ meV for Pt₄₀Co₃₉ yields the formation energy of L1₀ bulk PtCo alloy of $E^{MIX} = 4 * \varepsilon_{BOND}^{Pt-Co} = -121_{-24}^{+36}$ meV per atom, which is in agreement with the experimental value of $E^{MIX} = -140_{-22}^{+22}$ meV per atom.⁴⁶ The global minimum (Table 2, Figure 1) has the subsurface shell consisting exclusively of Co atoms, whereas the only present in this structure core site is occupied by a Pt atom. Most of the Pt atoms segregate on the surface, preferentially on corner and edge positions.

Pt₅₄Co₂₅. Descriptor contributions to E_{TOP} in the case of Pt₅₄Co₂₅ NPs (with Pt:Co ratio equals to approximately 2.2:1) has been calculated. The highest descriptor energy corresponds to Pt segregation on 7-coordinated edge positions (720 meV), and such segregation was also found to be favorable to 6-coordinated corner and 9-coordinated terrace sites (the energy gains being 523 and 415 meV, respectively). The relative energy contributions to E_{TOP} are 27%, 36% and 26%, respectively. Heteroatomic Pt-Co bonding has a 25 meV contribution per bond, which represents 10% contribution to E_{TOP} .

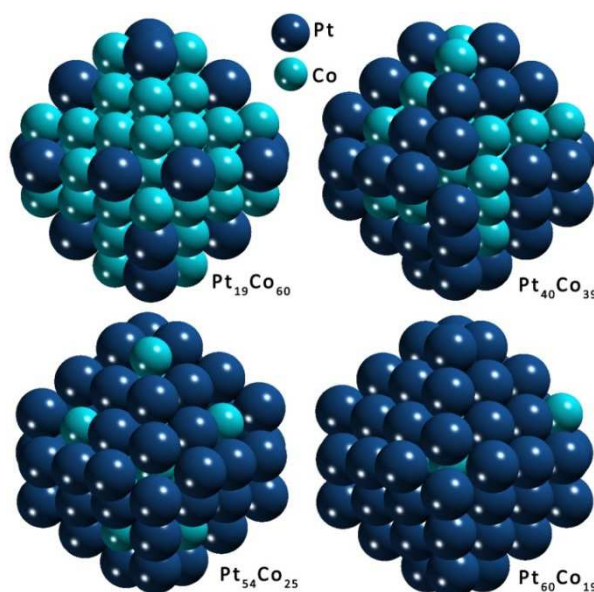


Figure 1. Exterior shells of the lowest-energy structure of Pt_xCo_{79-x} nanoparticles (19 ≤ X ≤ 60) according to results of density-functional calculations. The interior parts are not shown, since in all these particles they consist completely or almost completely (>95%) of cobalt atoms.

Pt₆₀Co₁₉. The analysis of the contribution of different descriptors to E_{TOP} for Pt₆₀Co₁₉ NPs showed that Pt is stabilized in any low-coordinated site compared to interior positions (Table 1). The highest

energy gain corresponds to 7-coordinated edge positions (714 meV), but the contributions are also high for 6-coordinated corner atoms (596 meV) and 9-coordinated terrace atoms (525 meV). The calculated respective contributions to the energy of the global minimum are 21%, 35%, and 32% (Figure 2). The energy for each of the heteroatomic Pt-Co bonds was calculated to be 35 meV, which adds up to ca. 11% of the overall stabilization. As one can see in Figure 1, in the global minimum structure the NP outer shell is almost fully composed of Pt (with only one Co atom occupying a corner position), whereas the interior consists of Co atoms (only one Pt atom is located in the center of the NP, Table 2).

In summary, our analysis showed that Pt clearly tends to occupy surface positions in 79 atom Pt-Co NP of any composition. Considering the contribution of different descriptors to E_{TOP} (Figure 2), we can state that $\varepsilon_{CORNER}^{Pt}$ and ε_{EDGE}^{Pt} ones are the most stabilizing. At the same time the contribution of $\varepsilon_{TERRACE}^{Pt}$ is found to be more important in Pt-rich NPs than in Co-rich ones, since the latter do not expose many terrace Pt atoms. Heteroatomic bonds give ca. 10-25% contribution. Note that all optimized Pt_xCo_{79-x} NPs exhibit the subsurface shell composed entirely of Co.

In order to evaluate the stability of NPs with $L1_0$ crystal structures, the term $\varepsilon_{LAYER} \sum_{LAYERS} |N_i^{Pt} - N_i^{Co}|$ was added to the topologic energy expression, where N_i^{Pt} and N_i^{Co} are the numbers of atoms of Pt and Co in the layer i of a NP and the sum is taken over all layers perpendicular to the {001} direction. The term $|N_i^{Pt} - N_i^{Co}|$ is larger when layers are composed entirely or mainly of Pt or Co and the term is closer to zero for layers composed of both elements in equal proportions. Therefore, the formation of a layered structure is favored, if $\varepsilon_{LAYER} < 0$.

Table 2. Structural characteristics of the most stable homotops with the lowest E_{ES} for different Pt_xCo_{79-x} and Pt_xCo_{140-x} truncated octahedral NPs. N_{BOND}^{Pt-Co} - number of heteroatomic bonds; N_{CORNER}^{Pt} , N_{EDGE}^{Pt} , $N_{TERRACE}^{Pt}$, $N_{SUBSURFACE}^{Pt}$, N_{CORE}^{Pt} - number of Pt atoms in corner, edge, terrace, subsurface and core positions, respectively. For every nanoparticle composition, the first row represents the absolute numbers, whereas the second row gives the relative percentage of the possible maximum value.

| | N_{BOND}^{Pt-Co} ^a | N_{CORNER}^{Pt} | N_{EDGE}^{Pt} | $N_{TERRACE}^{Pt}$ | $N_{SURFACE}^{Pt}$ ^b | $N_{SUBSURFACE}^{Pt}$ ^c | N_{CORE}^{Pt} ^c | $N_{INTERIOR}^{Pt}$ ^c |
|------------------------------------|---------------------------------|-------------------|-----------------|--------------------|---------------------------------|------------------------------------|------------------------------|----------------------------------|
| Pt ₁₉ Co ₆₀ | 115 | 12 | 7 | 0 | 19 | 0 | 0 | 0 |
| | 34% | 50% | 58% | 0% | 32% | 0% | 0% | 0% |
| Pt ₄₀ Co ₃₉ | 116 | 19 | 12 | 8 | 39 | 0 | 1 | 1 |
| | 35% | 79% | 100% | 33% | 65% | 0% | 100% | 5% |
| Pt ₅₄ Co ₂₅ | 128 | 22 | 12 | 20 | 54 | 0 | 0 | 0 |
| | 38% | 92% | 100% | 83% | 90% | 0% | 0% | 0% |
| Pt ₆₀ Co ₁₉ | 124 | 23 | 12 | 24 | 59 | 0 | 1 | 1 |
| | 37% | 96% | 100% | 100% | 98% | 0% | 100% | 5% |
| Pt ₉₆ Co ₄₄ | 244 | 24 | 24 | 44 | 92 | 0 | 4 | 4 |
| | 38% | 100% | 100% | 92% | 96% | 0% | 67% | 9% |
| Pt ₁₀₅ Co ₃₅ | 244 | 24 | 24 | 48 | 96 | 4 | 5 | 9 |
| | 38% | 100% | 100% | 100% | 100% | 11% | 83% | 20% |

^a The percentage of Pt-Co bonds is given with respect to the total number of bonds in the particle;

^b $N_{SURFACE}^{Pt} = N_{CORNER}^{Pt} + N_{EDGE}^{Pt} + N_{TERRACE}^{Pt}$ is the total number of Pt atoms on the surface;

^c $N_{INTERIOR}^{Pt}$ is the number of Pt atoms not exposed on the NP surface, $N_{SUBSURFACE}^{Pt}$ is the number of Pt atoms in the shell located immediately below the surface, and $N_{CORE}^{Pt} = N_{INTERIOR}^{Pt} - N_{SUBSURFACE}^{Pt}$.

However, the ε_{LAYER} values we obtained for $Pt_{40}Co_{39}$ NPs from the fitting process were in the range of 1-3 meV, i.e. negligible. For PdZn NPs,³² which were shown to have layered $L1_0$ structure, much larger in magnitude ε_{LAYER} descriptors of ca. 100 meV were obtained. Hence, for the Pt-Co NPs Monte-Carlo simulations with these extended topological energy expressions did not lead to $L1_0$ layered structures as global minima. Furthermore, we calculated the relative energy of a manually constructed $L1_0$ layered structure of $Pt_{40}Co_{39}$ NP and found that its energy was 4.6 eV higher than the global minimum we obtained. Our results clearly indicate that the formation of $L1_0$ layered structures is unfavorable compared to the $Pt_{\gamma}Co_{1-\gamma}$ -core@Co-rich-subsurface@Pt-shell structures obtained in our calculations.

Results for Pt_xCo_{140-x} nanoparticles

Furthermore, we analyzed the descriptor contributions for two different NPs of 140 atoms with Pt:Co ratios of approximately 2.2:1 and 3:1. In a previous study³² we analyzed the dependence of descriptors on the size for Au-Pd NPs and we obtained similar descriptor values for truncated octahedral *fcc* NPs of 79 and 140 atoms. Through the analysis of descriptors for Pt-Co NPs, we were able to evaluate how descriptors depend on the particle size in the case of a different nanoalloy, composed of elements with notably different atomic radii.

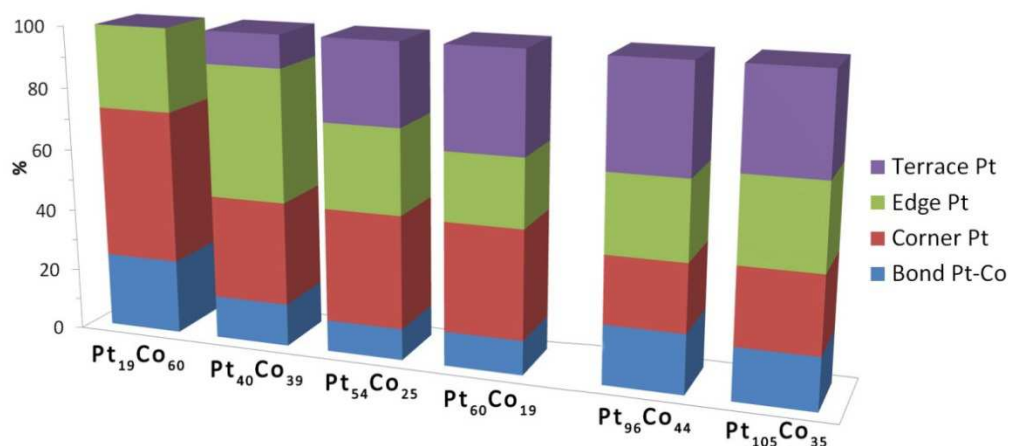


Figure 2. Relative energy contributions (%) to the global minima of Pt_xCo_{79-x} and Pt_xCo_{140-x} NPs according to the topologic energy expressions calculated as $\varepsilon_i N_i / \sum \varepsilon_i N_i$.

$Pt_{96}Co_{44}$. This composition was chosen to evaluate how the obtained global minimum is related to the hypothetical NP structure with seamless Pt shell, since there are in total 44 interior positions in the corresponding truncated octahedral *fcc* structure. The Pt:Co ratio is 2.2:1. The analysis of descriptor contributions to E_{TOP} for $Pt_{96}Co_{44}$ NP showed that like in the case of 79 atom NPs, Pt is stabilized in any surface site, when segregating on the surface from the interior. Just as in the 79 atom NP of similar Pt:Co ratio, $Pt_{54}Co_{25}$, the highest energy gain corresponds to 7-coordinated edge positions (680 meV), but the contributions are also high for 6-coordinated corner atoms (587 meV) and 9-coordinated terrace atoms (504 meV). The calculated respective contributions to the energy of the global minimum are 21%, 25%, and 34% (Figure 2). The energy lowering for one heteroatomic Pt-Co bond was calculated by E_{TOP} to be 51 meV; and this in overall represents a 19% contribution to the total energy. We can see in Figure 3 that the surface of the global minimum structure for $Pt_{96}Co_{44}$ is almost fully covered with platinum, that is, only 4 of the available 96 surface positions are occupied by cobalt atoms, whereas the subsurface shell consists of pure cobalt and NP core is Pt_4Co_2 . It is remarkable that some Pt atoms are located in the $Pt_{96}Co_{44}$ NP core despite that some terrace positions are still available for them. In consistence with the

descriptors showing that the energy gain corresponding to Pt segregation on surface sites follows the edge > corner > terrace order, those four surface Co atoms all occupy terrace positions.

Pt₁₀₅Co₃₅. We also performed the analysis of the chemical ordering in Pt₁₀₅Co₃₅ NPs with a 3:1 Pt:Co ratio, which is frequently used for materials that catalyze oxygen reduction reactions in fuel cells.^{47,48} Descriptor contributions are the highest in magnitude for the segregation of Pt on 7-coordinated edge positions (733 meV), followed by 6-coordinated corners (667 meV) and 9-coordinated terrace sites (464 meV). The relative contributions to the energy of the global minimum are 27%, 24%, and 31% (Figure 2). Pt-Co bond formation is characterized by 45 meV; which in overall gives 17% energy contribution. In the global minimum, the surface is fully covered with platinum, whereas the remaining Pt atoms are located either in the subsurface shell or the NP core. Note that the concentration of Pt in the core, 83%, is several times higher than in the subsurface shell, only 11%. The majority of Co atoms occupy subsurface positions with only one Co atom located in the core.

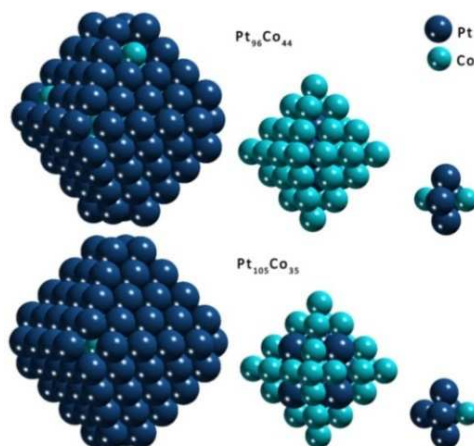


Figure 3. Surface shell, subsurface shell and core of the lowest-energy structures of the Pt₉₆Co₄₄ and Pt₁₀₅Co₃₅ nanoparticles according to results of density-functional calculations.

Descriptor dependence on the composition and nanoparticle size

One of the main objectives of this work is to assess how descriptors change as a function of both the Pt:Co content and the size of the NPs. This information is crucial, in particular when one needs to predict chemical ordering for larger NPs, electronic structure calculations of which still remain computationally unfeasible. The dependence of descriptors on the size and composition is presented in Figure 4.

One can instantly notice that descriptors substantially depend on the composition of the NP, that is, the binding in Co-rich NPs is quite different from that in Pt-rich NPs. In Co-rich NPs the heteroatomic bonds are stronger and the energy gain associated with surface segregation of Pt is also higher. However, changes in the absolute descriptor values do not lead to qualitatively different NP structures for different compositions. In all the analyzed NPs Pt definitely tends to occupy most of the surface positions, and edge and corner positions are preferred over terrace positions. Note that in practice the chemical ordering in Pt-Co nanoalloys may be affected by the reaction environment.^{17,18}

In order to explore the alloying effect on properties of Pt and Co components and to account for the observed descriptor dependence on NP composition, we have calculated variations of the average nearest neighbor interatomic distances and metal *d*-band center with the NP composition. Our results for the interatomic distances at all investigated nanoparticle stoichiometries show that Pt-Pt and Co-Co distances do not reveal any trend with increasing Pt concentration ($r(\text{Pt-Pt}) = 2.63\text{-}2.70 \text{ \AA}$ and $r(\text{Co-Co}) = 2.46\text{-}2.60 \text{ \AA}$). At the same time Pt-Co distances somewhat increase with Pt content ($r(\text{Pt-Co}) = 2.53\text{-}2.73$

Å), because Pt bonds with interior Co atoms dominant in Pt-rich NPs are longer than Pt bonds with surface Co atoms common in Co-rich NPs (Figure S1). This finding can account for the different descriptor values obtained (Figure 4) for Co-rich NPs compared with those of Pt-rich or 1:1 compositions. Note also that NPs with higher Pt content contain more of the longer Pt-Pt bonds and less of the shorter Co-Co bonds, so the overall NP size increases with growing Pt content.

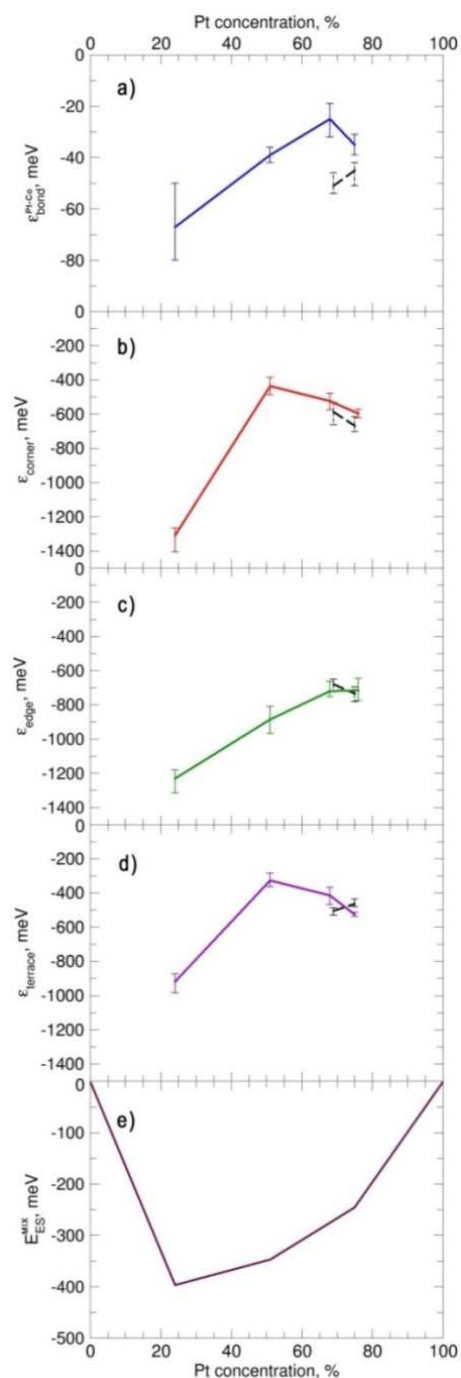


Figure 4. Dependence of a) $\varepsilon_{BOND}^{Pt-Co}$, b) $\varepsilon_{CORNER}^{Pt}$, c) ε_{EDGE}^{Pt} , d) $\varepsilon_{TERRACE}^{Pt}$ and e) ES calculated mixing energy per atom for Pt_xCo_{79-x} (colored lines) and Pt_xCo_{140-x} (dashed black lines) NPs on the Pt-Co composition. Error bars represent 60% confidence intervals of the ε_i calculated via the bootstrap analysis. If such confidence intervals for two ε_i values do not overlap, the probability that these descriptors are not different is less than $((1 - 0.6)/2)^2 = 4\%$.

Variation of Pt and Co *d*-band center positions with NP composition is directly related to the change in the adsorption properties of surface Pt atoms.⁴⁹ According to our calculated data, the Pt *d*-band center moves upwards, from -2.54 eV to -2.41 eV with the growing Pt-content in Pt_xCo_{79-x} NPs (Figure S2). To put the magnitude of this shift, 0.13 eV, in perspective we note that *d*-band center positions of Cu and Pt metals (with respect to the corresponding Fermi energies) differ by less than 0.1 eV.^{50,51} However, already this seemingly small difference can result in a very distinct catalytic activity. For instance, a shift of Pt *d*-band center in a Pt-Ni surface alloy vs. pure Pt by 0.16 eV was reported to correspond to the increase of the dissociative O₂ adsorption energy by almost 0.7 eV.⁴⁹ Detailed calculated data of the interatomic distances and *d*-band centers relative to the Fermi energies are provided in the Electronic Supplementary Information.

Another important measure of the binding strength of the alloying Pt and Co is their mixing energy (per atom), E^{MIX} . We calculated it for all Pt_xCo_{79-x} compositions as $E^{MIX} = [79 E(\text{Pt}_x\text{Co}_{79-x}) - X E(\text{Pt}_{79}) - (79 - X) E(\text{Co}_{79})] / 79^2$, where $E(\text{Pt}_x\text{Co}_{79-x})$ is the total energy of the Pt_xCo_{79-x} NP and $E(\text{Pt}_{79})$, $E(\text{Co}_{79})$ are the energies of the respective monometallic NPs with the same structure calculated with the same plane-wave basis as that for the Pt_xCo_{79-x} NP. The minimum of ES mixing energies (≈ -390 meV) corresponds to 1:3 Pt:Co ratio. The latter is related to the fact that in Co-rich the NPs all Pt atoms segregate on corner and edge positions, causing a very strong stabilization reflected in the lowest mixing energy. Similar mixing energies (≈ -300 meV) were calculated by Noh et al. for 0.7-1.5 nm Pt-Co NPs.³¹

Our results show that the dependence of the descriptors on the NP size is almost within the statistical accuracy of the calculations and hence in the first approximation it can be neglected. This is in line with previous findings that (with few exceptions) other physical properties of NPs larger than 1.5 nm already depend rather smoothly on their size and start to converge to a certain value.^{36,37,53} Therefore, we find appropriate to use the descriptors determined for particles of 1-2 nm for reliable predictions of the chemical ordering in (much) bigger NPs. Note, however, that the dependence of chemical and catalytic properties on the size of transition metal or oxide NPs is notably more complicated.⁵⁴⁻⁵⁶

Table 3. Structural properties of the most stable homotops with the lowest E_{ES} for different Pt_xCo_{1463-x} truncated octahedral NPs. N_{BOND}^{Pt-Co} = number of heteroatomic bonds; N_{CORNER}^{Pt} , N_{EDGE}^{Pt} , $N_{TERRACE}^{Pt}$, $N_{SUBSURFACE}^{Pt}$, N_{CORE}^{Pt} = number of Pt atoms in corner, edge, terrace, subsurface and core positions, respectively. For every NP composition, the first row represents the absolute numbers, whereas the second row is the relative percentage of the maximum value.

| | N_{BOND}^{Pt-Co} ^a | N_{CORNER}^{Pt} | N_{EDGE}^{Pt} | $N_{TERRACE}^{Pt}$ | $N_{SURFACE}^{Pt}$ ^b | $N_{SUBSURFACE}^{Pt}$ ^c | N_{CORE}^{Pt} ^c | $N_{INTERIOR}^{Pt}$ ^c |
|--|---------------------------------|-------------------|-----------------|--------------------|---------------------------------|------------------------------------|------------------------------|----------------------------------|
| Pt₃₆₆Co₁₀₉₇ | 1922 | 24 | 98 | 244 | 366 | 0 | 0 | 0 |
| | 25% | 100% | 91% | 55% | 64% | 0% | 0% | 0% |
| Pt₇₃₂Co₇₃₁ | 3546 | 24 | 108 | 408 | 540 | 32 | 160 | 192 |
| | 46% | 100% | 100% | 93% | 94% | 8% | 33% | 22% |
| Pt₁₀₀₃Co₄₆₀ | 3864 | 24 | 108 | 440 | 572 | 162 | 269 | 431 |
| | 50% | 100% | 100% | 100% | 100% | 40% | 55% | 48% |
| Pt₁₀₉₇Co₃₆₆ | 3524 | 24 | 108 | 440 | 572 | 184 | 341 | 525 |
| | 45% | 100% | 100% | 100% | 100% | 46% | 70% | 59% |

^a The percentage of Pt-Co bonds is given with respect to the total number of bonds in the NP; ^b $N_{SURFACE}^{Pt} = N_{CORNER}^{Pt} + N_{EDGE}^{Pt} + N_{TERRACE}^{Pt}$ is the total number of Pt atoms on the surface; ^c $N_{INTERIOR}^{Pt}$ is the number of Pt atoms not exposed on the NP surface, $N_{SUBSURFACE}^{Pt}$ is the number of Pt atoms in the shell located immediately below the surface and $N_{CORE}^{Pt} = N_{INTERIOR}^{Pt} - N_{SUBSURFACE}^{Pt}$.

Chemical ordering in Pt-Co nanoparticles formed of 1463 atoms

In particular, we used the descriptor values obtained for $\text{Pt}_x\text{Co}_{79-x}$ and $\text{Pt}_x\text{Co}_{140-x}$ NPs for bigger ≈ 4 nm $\text{Pt}_x\text{Co}_{1463-x}$ particles. The chemical ordering was optimized in $\text{Pt}_{366}\text{Co}_{1097}$, $\text{Pt}_{732}\text{Co}_{731}$, $\text{Pt}_{1003}\text{Co}_{460}$ and $\text{Pt}_{1097}\text{Co}_{366}$ NPs with Pt:Co ratios of 1:3, 1:1, 2.2:1 and 3:1, respectively. The application of descriptors derived for smaller NPs to large species is possible only when their shape is preserved. This causes a certain discrepancy between the octahedral shape of the considered ≈ 4 nm large models and the more spherical shape of experimentally observed NPs (discussed later). Nevertheless, this discrepancy does not seem to be critical as it does not affect the agreement between experimental and theoretical results.

As can be seen from the results in Table 3 and Figure 5, the surfaces of $\text{Pt}_{1003}\text{Co}_{460}$ and $\text{Pt}_{1097}\text{Co}_{366}$ NPs are fully formed of platinum, and cobalt only occupies interior positions, consistent with the picture we obtained for smaller NPs. Note that the concentration of Pt in subsurface shells of these NPs is always notably lower than in their core. Even in the Co-rich NP $\text{Pt}_{366}\text{Co}_{1097}$, all the corners and most of the edges are occupied by Pt atoms and surface Co atoms occupy mostly terrace positions.

The chemical ordering of the $\text{Pt}_x\text{Co}_{1463-x}$ NPs presented in Table 3 and Figure 5 is optimized using the descriptors set for $\text{Pt}_x\text{Co}_{79-x}$ NPs. Notably, the chemical ordering calculated with the descriptors obtained for $\text{Pt}_x\text{Co}_{140-x}$ NPs reveals only minor differences. For both $\text{Pt}_{1003}\text{Co}_{460}$ and $\text{Pt}_{1097}\text{Co}_{366}$ species the skin fully consists of Pt atoms, independently of whether the descriptors for $\text{Pt}_x\text{Co}_{79-x}$ or $\text{Pt}_x\text{Co}_{140-x}$ were used.

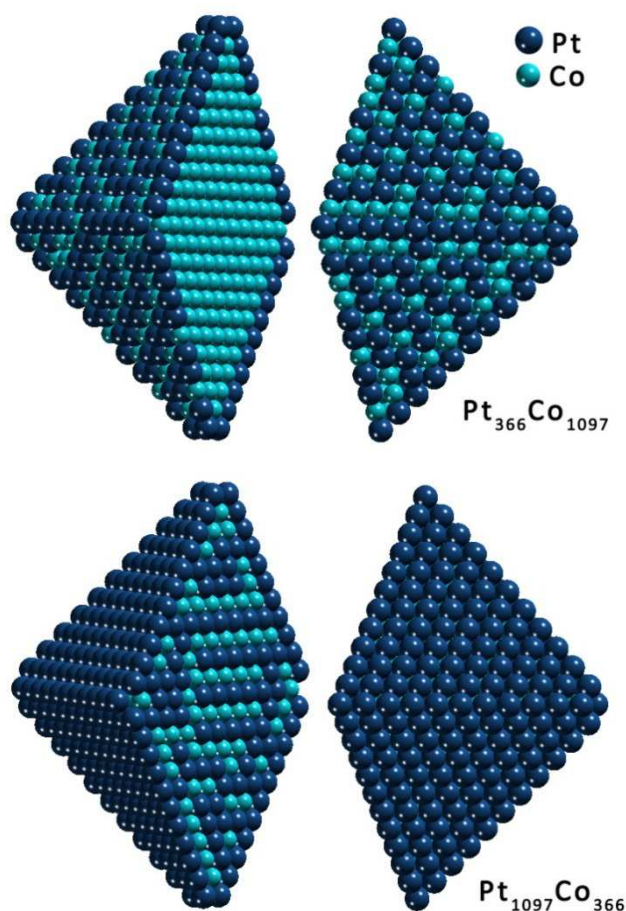


Figure 5. The structures of $\text{Pt}_{366}\text{Co}_{1097}$ NPs and $\text{Pt}_{1097}\text{Co}_{366}$ with optimized chemical ordering.

For a particular case of NPs with equal proportions of Pt and Co, we performed a more thorough investigation at various nanoparticle sizes. From the results in Figure 6 one can see that NP edges are populated solely by Pt already in NPs of ≈ 1 nm, whereas full occupation of corner sites by Pt is achieved in 2 nm large species. The majority of terrace sites are also occupied by Pt for NPs larger than 2 nm. However, an outer Pt shell is not formed even in ≈ 4.5 nm NPs – there is always a small fraction of Co on the surface. The reason for the delayed surface saturation by Pt can be seen in the composition of the interior region. According to our calculations, in the core-shell NPs Pt concentration is less than 10% in the subsurface shell, whereas in the core it is around 32%. Such a significant amount of Pt in the core does not leave enough Pt to fill all surface positions. Hence, for equiatomic Pt-Co NPs we predict the emergence of Pt₁Co₂-core@Co-rich-subsurface@Pt-rich-shell structures at sizes between 2 and 5 nm.

Note that on the one hand the employed method may account for *mechanical* relaxation and associated stress or strain in large NPs only in an indirect way. On the other hand, the used approach is powerful enough to reliably describe the underlying *chemical* driving forces leading to the formation of Pt₁Co₂ composition of NP core instead of purely Co core. Hence, we trust the validity of the presented results, even if they are based on the extrapolation of DFT data computed for smaller NPs. Our results for Pt_xCo_{79-x} and Pt_xCo_{140-x} NPs, for which explicit DFT calculations are performed, also support the emergence of the Pt_yCo_{1-y}-core@Co-rich-subsurface@Pt-shell arrangements as the most thermodynamically stable ones. Indeed, such NPs as Pt₄₀Co₃₉, Pt₆₀Co₁₉ and Pt₉₆Co₄₄ feature some Pt atoms in the core region when there are available sites for Pt on the terraces. Concomitantly, subsurface shells of such NPs are commonly composed solely of Co.

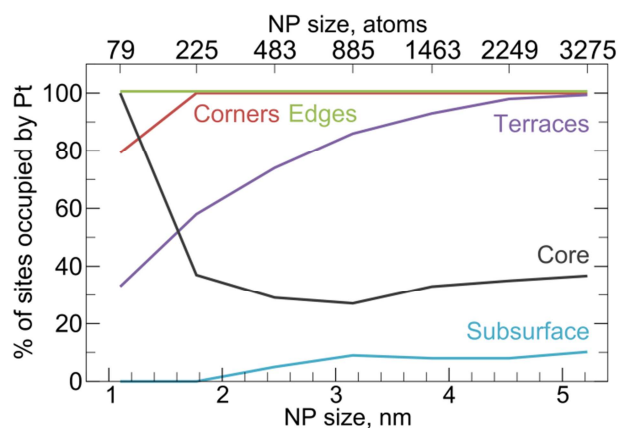


Figure 6. Distribution of Pt atoms among various sites of 1:1 Pt:Co nanoparticles as a function of the particle size. Core encompasses all atoms located in neither the surface nor the first subsurface shells.

Structure of PtCo nanoparticles revealed by X-ray photoelectron spectroscopy

In order to experimentally verify the formation of a thermodynamically stable Pt-Co core-shell structure, we prepared a 10 nm thick Pt:Co = 1:1 film on a glassy carbon substrate. The TEM cross-view image of the film presented in Figure 7 shows the formation of almost spherical NPs of about 8 nm in size. The sample stoichiometry (1:1) was determined by the energy dispersive X-ray (EDX) spectroscopy. Atomic Force Microscopy (AFM) analysis demonstrates a nano-granular structure of the catalyst films formed by NPs that was preserved during the sample annealing, see Figure S3 of the annealed film in the Electronic Supplementary Information.

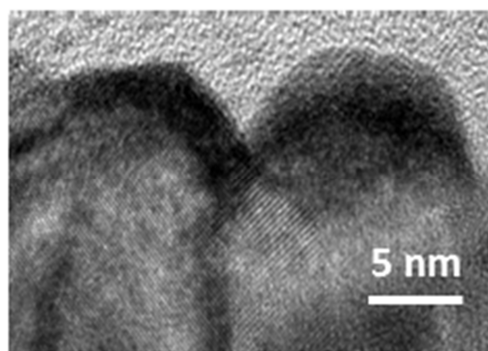


Figure 7. High resolution TEM cross-view image of the PtCo film.

Recently, it has been demonstrated that photoelectron spectroscopy at variable photon energy can be successfully used for non-destructive depth profiling of bimetallic catalyst NPs.⁵⁷ In the present work we used soft X-ray (SXPS) and hard X-ray (HAXPES) synchrotron radiation photoelectron spectroscopy of the Pt 4f and Co 3p emission for Pt and Co depth profiling. Figure 8 shows the photoemission spectra obtained at excitation energies $E_{h\nu} = 180, 650$ eV and 5950 eV. The PtCo samples were investigated as prepared and after vacuum annealing at 770 K for 10 minutes. The peak at binding energy (BE) of 58.5 eV corresponds to metallic (or alloyed) cobalt, whilst cobalt oxide would be seen at 60.5 eV.^{58,59} The doublet at 71.1 – 74.4 eV is associated with Pt 4f_{7/2-5/2} emission.⁶⁰ By considering the effective escape depth, usually called as photoelectron inelastic mean free path (IMFP) $\lambda(E_A)$, the probability P that an electron can escape without energy loss can be expressed as $P = \exp[-d/(\lambda(E_A)\cos\alpha)]$, where d is the escaping depth, α is the angle of emission of the detected electrons with respect to the surface normal and E_A is the kinetic energy of an electron excited from the level A.⁶¹ The so-called sampling depth $D = 3\lambda\cos\alpha$ corresponds to the surface layer in which 95% of the detected electrons is produced. $\lambda(E_A)$ values and consequently the sampling depth can be determined using the so-called TPP2M formula.⁶² For example, in the case of the used excitation energies, Pt 4f photoelectrons travelling in Pt exhibit $\lambda_{Pt} = 3.8, 8.3$ and 47 Å, respectively. In general, in the range of energies we used the sampling depth increased with the photon energy $E_{h\nu}$ and therefore with E_A ($E_A = E_{h\nu} - BE_A$).

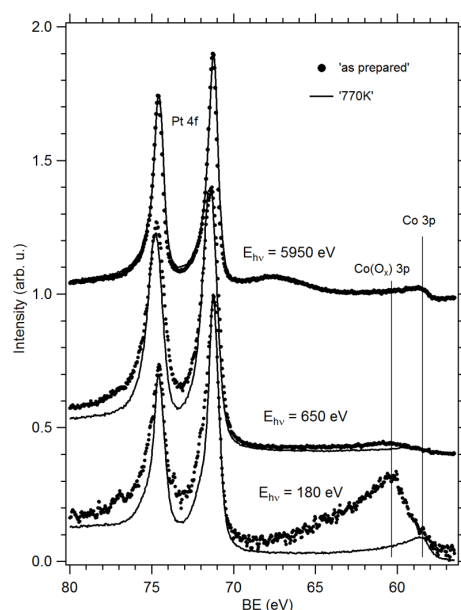


Figure 8. SXPS and HAXPES Pt 4f and Co 3p spectra of the magnetron sputtered PtCo film and the film annealed at 770 K for 10 min.

For a simple evaluation of the average Pt:Co concentration ratios n_{Pt}/n_{Co} in the probed surface region, we used experimentally determined ratios of Pt 4f and Co 3p peak areas I_{Pt}/I_{Co} by applying calculated photon energy dependent Pt 4f and Co 3p photoelectron excitation cross-sections $\sigma_{Pt\ 4f}(E_{h\nu})$ and $\sigma_{Co\ 3p}(E_{h\nu})$.^{63,64} We considered the PtCo sample as a homogenous alloy, whereas $\lambda_{Pt,Co}$ and the analyzer transmission function (proportional to $1/E$) were assumed to be constant because of the similar values of binding energies for Pt and Co, E_{Pt} and E_{Co} :

$$\frac{n_{Pt}}{n_{Co}} = \frac{I_{Pt}}{\sigma_{Pt}} \frac{\sigma_{Co}}{I_{Co}} \quad (3).$$

The cross-sections σ_{Co} and σ_{Pt} and Pt:Co concentration ratios n_{Pt}/n_{Co} are listed in Table 4.

Table 4. Co 3p and Pt 4f photoionization cross sections ($\sigma_{Co\ 3p}$ and $\sigma_{Pt\ 4f}$)^{62,63} and Pt:Co concentration ratios (n_{Pt}/n_{Co}) determined for the as prepared and annealed PtCo films as a function of the photon energy $E_{h\nu}$ and/or the sampling depth D .

| $E_{h\nu}(eV) / D(\text{\AA})$ | $\sigma_{Co\ 3p}$ | $\sigma_{Pt\ 4f}$ | n_{Pt}/n_{Co} | |
|--------------------------------|-------------------|-------------------|-----------------|----------|
| | | | As prepared | Annealed |
| 180 / 11 | 0.922 | 2.28 | 0.98 | 3.20 |
| 650 / 25 | 0.17 | 2.06 | 1.77 | 2.59 |
| 5950 / 140 | -- | -- | 1.00 | 1.00 |

The Pt:Co concentration ratios in Table 4 clearly show that for the annealed PtCo film the surface region is rich in Pt and the relative Pt concentration decreases with D (we note that in the case of non-homogeneous samples mainly the topmost surface layer contributes to the detected photoemission signal). In the case of the as prepared sample the situation is different, and for the most surface sensitive case we can observe higher Co concentration. This difference can be explained by the formation of a topmost cobalt oxide thin film covering the Pt-rich subsurface, since the oxidized Co can be clearly seen from the Co 3p spectra recorded for the as prepared sample at the highest surface sensitivity ($E_{h\nu} = 180$ eV, Figure 8), while only metallic Co is observed after annealing.

Surface sensitive SXPES analysis showed that sample annealing led to the redistribution of the Pt and Co concentration profiles, see Table 4, i.e. that n_{Pt}/n_{Co} was treatment dependent. On the other hand, bulk sensitive HAXPES did not reveal any variation in the Pt:Co concentration ratio: the spectra measured before and after annealing were identical and the integral concentrations of Pt and Co were constant, see Figure 8 and Table 4. Moreover, no CoO_x intensity was detected by the bulk sensitive HAXPES in the case of the as prepared sample, confirming that Co oxide seen in the SXPES Co 3p spectrum was present in the form of a very thin surface overlayer.

The HAXPES data clearly shows that the total cobalt concentration does not change in the sample during the annealing process. It indicates that no Co was removed, e.g. as volatile oxide species. In fact, thermal decomposition of the CoO_x species takes place during the annealing. This result is confirmed by the O 1s SXPES spectra before and after annealing (Electronic Supplementary Information, Figure S4), where the O 1s peak in the "as prepared" spectrum disappeared during the sample annealing.

We cannot use HAXPES data for the Pt:Co concentration ratio calculation, since reliable data of photoemission cross sections are not available. However, the identical shape of the Pt 4f – Co 3p spectra before and after annealing indicates a constant I_{Pt}/I_{Co} ratio and can be explained by both the high

sampling depth and the conservation of the integral values of Pt and Co concentrations. Hence, surface redistribution of Pt and Co concentrations cannot be detected in this case. We can set the Pt and Co concentration ratio to the default value of 1, as the Pt:Co integral stoichiometry (1:1) is known from the quantitative EDX analysis.

The simple depth profiling presented above gave us a rough picture of PtCo core – Pt shell structure formed upon vacuum annealing; however, for the experimental verification of the theoretical model of the Pt-Co nanoparticles with one monolayer thick Pt skin (shell) coating Pt-Co alloy we had to perform a precise quantitative analysis of the photoemission data. We calculated the signal intensity ratios Y_{Pt}/Y_{Co} that would be detected by the spectrometer for single layer Pt skin - PtCo_x core particles and compared them with measured experimental values I_{Pt}/I_{Co} . In agreement with the TEM and AFM analysis, we considered the particle diameter of 8 nm and we approximated their shapes by hemispherical structures.

For Pt_xCo_y particles in the form of a core alloy covered by a Pt monolayer of thickness d_{Pt} (2.8 Å), a relative core Co concentration \tilde{n}_{Co} can be determined by calculating the number of Pt atoms "consumed" for the Pt skin formation and by considering the total number of Pt and Co atoms in the particle. The Co photoemission signal Y_{Co}^{α} detected by the analyzer can then be calculated using the formula

$$Y_{Co}^{\alpha} = FT(E_{Co})\sigma_{Co}(E_{hv})\tilde{n}_{Co} \left[\int_0^{\infty} \exp\left(-\frac{z}{\lambda_{CoPt}(E_{Co})\cos\alpha}\right) dz \right] \exp\left(-\frac{d_{Pt}}{\lambda_{Pt}(E_{Co})\cos\alpha}\right) \quad (4).$$

Here $\lambda_{CoPt}(E_{Co})$ and $\lambda_{Pt}(E_{Co})$ are IMFPs of the Co 3p photo-excited electrons travelling in the Pt_xCo_y alloy and in the Pt overlayer, respectively, and α is the emission angle. F is the photon flux and T is the analyzer transmission function. In case of Y_{Pt}^{α} the signal is composed of two parts, Pt 4f emission from the core Pt_yCo_{1-y} alloy and from the Pt skin:

$$Y_{Pt}^{\alpha} = FT(E_{Pt})\sigma_{Pt}(E_{hv}) \left[\int_0^{d_{Pt}} \exp\left(-\frac{z}{\lambda_{Pt}(E_{Pt})\cos\alpha}\right) dz + \tilde{n}_{Pt} \int_{d_{Pt}}^{\infty} \exp\left(-\frac{z}{\lambda_{CoPt}(E_{Pt})\cos\alpha}\right) dz \right] \quad (5).$$

Similarly, $\lambda_{CoPt}(E_{Pt})$ and $\lambda_{Pt}(E_{Pt})$ are IMFPs of the Pt 4f photo-excited electrons travelling in the Pt_yCo_{1-y} alloy and the Pt overlayer, respectively. \tilde{n}_{Pt} is the Pt concentration in the core calculated in a similar way as \tilde{n}_{Co} above. We assume Pt skin to have thickness $d_{Pt} = 2.8$ Å and Pt concentration of 1. Since the Pt 4f and Co 3f electrons are collected simultaneously, F is constant and $T(E) = K/E$, where K is an analyzer transmission constant. In the case of spherical particles, the emission angle α is a parameter dependent on the escaping beam position and the total value of Y can be obtained by numerically integrating Y^{α} over the hemispherical particle surface with the variable α (0 – 90 degrees) depending on the distance from the particle centre. By calculating the Y_{Pt}/Y_{Co} ratio, the unknown parameters F and the transmission coefficient K are eliminated.

Table 5. Detected (I_{Pt}/I_{Co}) and calculated (Y_{Pt}/Y_{Co}) photoemission intensity ratios obtained at different excitation energies E_{hv} .

| $E_{hv}(eV)$ | I_{Pt}/I_{Co} | Y_{Pt}/Y_{Co} |
|--------------|-----------------|-----------------|
| 180 | 7 | 12 |
| 650 | 29 | 31 |

In Table 5 we compared the detected signal ratios with the calculated ones. There is a generally good agreement, particularly for higher photon energies. The reason for somewhat larger calculated values Y_{Pt}/Y_{Co} may be related to neglecting the presence of the subsurface Co-rich shell predicted by the DFT calculations in our XPS analysis. Consideration of a Co-rich subsurface region should slightly increase the Co signal Y_{Co} at the expense of Y_{Pt} and therefore make Y_{Pt}/Y_{Co} smaller relative to the simpler case of just Pt-Co core and Pt shell. This effect would be more notable for lower photon energies.

By comparing the aforementioned calculations with experimental photoemission depth profiling we can conclude that the model of spherical alloy particles formed by a homogeneous Pt_xCo_{1-y} alloy covered by a monolayer Pt skin corresponds very well to the real structure of PtCo thin films. It is also in agreement with the PtCo particle structure obtained by DFT calculations presented in this work. The difference between the sizes of real nanoparticles (larger) and those considered by theory (smaller) appears to be not critical, because it is expected that the thermodynamically equilibrated structure observed for large particles should be even more easily obtained for smaller ones.

Conclusions

We have comprehensively analyzed near-surface chemical ordering in Pt-Co nanoparticles, which represent materials of major importance in catalysis and other applications. For the analysis we applied a method recently developed by some of us, which is based on topological energy expressions that depend on the mutual positions of Co and Pt atoms in the NP structure. The energetic parameters (descriptors) in the topological energy expressions were fitted to the energy of a series of low-energy Pt-Co NPs structurally optimized by DFT calculations. The effect of alloying on the geometric and electronic structures of the NPs was also analyzed.

More specifically, we calculated the optimal chemical ordering in Pt_xCo_{79-x} NPs with four different compositions 1:3, 1:1, 2.2:1 and 3:1; the same method was also applied for larger Pt_xCo_{140-x} NPs with Pt:Co ratios 2.2:1 and 3:1. The generated descriptors (parameters in the topological energy expressions) were found not to depend strongly on the NP size, therefore it was possible to apply the descriptors obtained for 1-2 nm particles for the optimization of notably larger Pt_xCo_{1463-x} species. Our results show that independently of the size and composition of the Pt-Co NPs, Pt tends to segregate on the surface and prefers to occupy corner and edge positions, whereas surface Co atoms tend to occupy terraces. The subsurface shell was found to be almost purely Co in most of the cases, whereas the core of the NPs contained Pt atoms even when some terrace positions were available for them. These results were supported by X-ray photoelectron spectroscopy experiments performed on Pt-Co nanoparticles with various photon energies and information depths. Contrary to some previous experiments or computational studies based on interatomic potentials, the formation of Pt-Co NPs with layered $L1_0$ structures was not found to be favorable. The chemical ordering in the lowest-energy Pt-Co NPs can be described as a *Pt_yCo_{1-y}-core@Co-rich-subsurface@Pt-rich-shell* structure. The latter result obtained by this powerful method deepens the understanding of the structure of highly important Pt-Co nanomaterials.

Acknowledgements

This study was supported by the European Commission (FP7-NMP.2012.1.1-1 project ChipCAT, Ref. Nº 310191 and COST Action MP0903 "Nanoalloy"), the Spanish MINECO (grant CTQ2012-34969) and the Generalitat de Catalunya (projects 2014SGR97 and XRQTC). Financial support from the Spanish MEDU is gratefully acknowledged by SMK (FPU grant AP2009-3379). The authors acknowledge financial support by the Czech Science Foundation under project GA CR 13-10396S. The authors are grateful to the Red Española de Supercomputación for provided computer resources and technical assistance.

Electronic Supplementary Information (ESI) available: Graphs of the calculated average interatomic distances and d -band center positions in Pt-Co nanoparticles. AFM images and XPS O 1s spectra of prepared by magnetron sputtering films of Pt-Co nanoparticles.

References:

- ¹ D. Sellmyer and R. Skomski, *Advanced Magnetic Nanostructures*, Springer, NewYork, 2006.
- ² J. Park, M. G. Kim, Y. Jun, J. S. Lee, W. Lee and J. Cheon, *J. Am. Chem. Soc.*, 2004, **126**, 9072.
- ³ S. Sun, C. B. Murray, D. Weller, L. Folks and A. Moser, *Science*, 2000, **287**, 1989.
- ⁴ D. J. Sellmyer, Y. Xu, M. Yan and R. Skomski, *IEEE Trans. Magn.*, 2005, **41**, 560.
- ⁵ J. Bartolomé, L. M. García, F. Bartolomé, F. Luis, F. Petroff, C. Deranlot, F. Wilhelm and A. Rogalev, *J. Magn. Magn. Mater.*, 2007, **316**, e9.
- ⁶ F. J. Lai, L. S. Sarma, H. L. Chou, D. G. Liu, C. A. Hsieh, J. F. Lee and B. J. Hwang, *J. Phys. Chem. C*, 2009, **113**, 12674.
- ⁷ R. Loukrakpam, S. Shan, V. Petkov, L. Yang, J. Luo and C.-J. Zhong, *J. Phys. Chem. C*, 2013, **117**, 20715.
- ⁸ V. R. Stamenkovic, B. S. Mun, M. Arenz, K. J. J. Mayrhofer, C. A. Lucas, G. Wang, P. N. Ross and N. M. Markovic, *Nat. Mater.*, 2007, **6**, 241.
- ⁹ D. Schanke, S. Vada, E. A. Blekkan, A. M. Hilmen, A. Hoff and A. Holmen, *J. Catal.*, 1995, **156**, 85.
- ¹⁰ S. Vada, A. Hoff, E. Adnanes, D. Schanke and A. Holmen, *Top. Catal.*, 1995, **2**, 155.
- ¹¹ D. Wang, H. L. Xin, R. Hovden, H. Wang, Y. Yu, D. A. Muller, F. J. DiSalvo and H. D. Abruña, *Nat. Mater.*, 2013, **12**, 81.
- ¹² R. Fiala, M. Vaclavu, M. Vorokhta, I. Khalakhan, J. Lavkova, V. Potin, I. Matolinova and V. Matolin, *J. Power Sources*, 2015, **273**, 105.
- ¹³ R. Tsukamoto, M. Muraoka, M. Seki, H. Tabata and I. Yamashita, *Chem. Mater.*, 2007, **19**, 2389.
- ¹⁴ F. Tournus, A. Tamion, N. Blanc, A. Hannour, L. Bardotti, B. Prével, P. Ohresser, E. Bonet, T. Epicier and V. Dupuis, *Phys. Rev. B*, 2008, **77**, 144411.
- ¹⁵ J. Kim, C. Rong, Y. Lee, J. P. Liu and S. Sun, *Chem. Mater.*, 2008, **20**, 7242.
- ¹⁶ J.-Y. Bigot, H. Kesserwan, V. Halté, O. Ersen, M. S. Moldovan, T. H. Kim, J.-T. Jang and J. Cheon, *Nano Lett.*, 2012, **12**, 1189.
- ¹⁷ K. J. J. Mayrhofer, V. Juhart, K. Hartl, M. Hanzlik and M. Arenz, *Angew. Chem. Int. Ed.*, 2009, **48**, 3529.
- ¹⁸ H. L. Xin, S. Alayoglu, R. Tao, A. Genc, C.-M. Wang, L. Kovarik, E. A. Stach, L.-W. Wang, M. Salmeron, G. A. Somorjai and H. Zhong, *Nano Lett.*, 2014, **14**, 3203.
- ¹⁹ R. Ferrando, J. Jellinek and R. L. Johnston, *Chem. Rev.*, 2008, **108**, 845.
- ²⁰ S. Heiles and R. L. Johnston, *Int. J. Quantum Chem.*, 2013, **113**, 2091.
- ²¹ Y. H. Chui and K.-Y. Chan, *Chem. Phys. Lett.*, 2005, **408**, 49.
- ²² G. Rossi, R. Ferrando and C. Mottet, *Faraday Discuss.*, 2008, **138**, 193.
- ²³ F. Calvo and C. Mottet, *Phys. Rev. B*, 2011, **84**, 035409.
- ²⁴ A. Demortiere and C. Petit, *Langmuir*, 2007, **23**, 8575.
- ²⁵ J. Penuelas, P. Andreatza, C. Andreatza-Vignolle, H. C. N. Tolentino, M. De Santis and C. Mottet, *Phys. Rev. Lett.*, 2008, **100**, 115502.
- ²⁶ L. Favre, V. Dupuis, E. Bernstein, P. Melinon, A. Pérez, S. Stanescu, T. Epicier, J. P. Simon, D. Babboneau, J. M. Tonnerre and J. L. Hodeau, *Phys. Rev. B*, 2006, **74**, 014439.
- ²⁷ L. J. Qin, Y. H. Zhang, S. P. Huang, H. P. Tian and P. Wang, *Phys. Rev. B*, 2010, **82**, 075413.
- ²⁸ I. Parsina, C. DiPaola and F. Baletto, *Nanoscale*, 2012, **4**, 1160.
- ²⁹ R. V. Chepulska and W. H. Butler, *Phys. Rev. B*, 2012, **86**, 155401.
- ³⁰ W. F. Hu, H. K. Yuan, H. Chen, G. Z. Wang and G. L. Zhang, *Phys. Lett. A*, 2014, **378**, 198.
- ³¹ S. H. Noh, M. H. Seo, J. K. Seo, P. Fischer and B. Han, *Nanoscale*, 2013, **5**, 8625.
- ³² S. M. Kozlov, G. Kovács, R. Ferrando and K. M. Neyman, *Chem. Sci.*, 2015, **6**, doi: 10.1039/c4sc03321c.

- ³³ P. Wessa, 2015, Free Statistics Software, Office for Research Development and Education, version 1.1.23-r7, URL <http://www.wessa.net/>
- ³⁴ K. M. Neyman, R. Sahnoun, C. Inntam, S. Hengrasmee and N. Rösch, *J. Phys. Chem. B*, 2004, **108**, 5424.
- ³⁵ F. Viñes, F. Illas and K. M. Neyman, *Angew. Chem. Int. Ed.*, 2007, **46**, 7094.
- ³⁶ A. Roldán, F. Viñes, F. Illas, J. M. Ricart and K. M. Neyman, *Theor. Chem. Acc.*, 2008, **120**, 565.
- ³⁷ L. Li, A. H. Larsen, N. A. Romero, V. A. Morozov, C. Glinsvad, F. Abild-Pedersen, J. Greeley, K. W. Jacobsen and J. K. Nørskov, *J. Phys. Chem. Lett.*, 2013, **4**, 222.
- ³⁸ A. C. Davison and D. V. Hinkley, *Bootstrap Methods and their Application*, University Press, Cambridge, 1997.
- ³⁹ G. Kresse and J. Furthmüller, *Phys. Rev. B*, 1996, **54**, 11169.
- ⁴⁰ J. P. Perdew, K. Burke and M. Ernzerhof, *Phys. Rev. Lett.*, 1996, **77**, 3865.
- ⁴¹ P. Janthon, S. M. Kozlov, F. Viñes, J. Limtrakul and F. Illas, *J. Chem. Theory Comput.*, 2013, **9**, 1631.
- ⁴² P. Janthon, S. A. Luo, S. M. Kozlov, F. Viñes, J. Limtrakul, D. G. Truhlar and F. Illas, *J. Chem. Theory Comput.*, 2014, **10**, 3832.
- ⁴³ P. E. Blöchl, *Phys. Rev. B*, 1994, **50**, 17953.
- ⁴⁴ M. Methfessel and A. T. Paxton, *Phys. Rev. B*, 1989, **40**, 3616.
- ⁴⁵ S. M. Kozlov, H. A. Aleksandrov, J. Goniakowski and K. M. Neyman, *J. Chem. Phys.*, 2013, **139**, 084701.
- ⁴⁶ R. Hultgren, P. D. Desai, D. T. Hawkins, M. Gleiser and K. K. Kelley, *Selected Values of Thermodynamic Properties of Binary Alloys*, American Society for Metals, Metals Park, Ohio, 1973.
- ⁴⁷ S. Siracusano, A. Stassi, V. Baglio, A. S. Aricò, F. Capitanio and A. C. Tavares, *Electrochim. Acta*, 2009, **54**, 4844.
- ⁴⁸ T. Lopes, E. Antolini, F. Colmati and E. R. Gonzalez, *J. Power Res.*, 2007, **164**, 111.
- ⁴⁹ J. K. Nørskov, T. Bligaard, J. Rossmeisl and C. H. Christensen, *Nat. Chem.*, 2009, **1**, 37.
- ⁵⁰ A. Notario-Estévez, S. M. Kozlov, F. Viñes and F. Illas, *Chem. Commun.*, 2015, **51**, DOI: 10.1039/C4CC10427G.
- ⁵¹ A. Vojvodic, J. K. Nørskov and F. Abild-Pedersen, *Top. Catal.*, 2014, **57**, 25.
- ⁵² S. M. Kozlov, H. A. Aleksandrov and K. M. Neyman, *J. Phys. Chem. C*, 2014, **118**, 15242.
- ⁵³ S. M. Kozlov and K. M. Neyman, *Top. Catal.*, 2013, **56**, 867.
- ⁵⁴ H. A. Aleksandrov, S. M. Kozlov, S. Schauer mann, G. N. Vayssilov and K. M. Neyman, *Angew. Chem. Int. Ed.*, 2014, **53**, 13371.
- ⁵⁵ S. M. Kozlov, H. A. Aleksandrov and K. M. Neyman, *J. Phys. Chem. C*, 2015, **119**, 5180.
- ⁵⁶ M. A. Sk, S. M. Kozlov, K. H. Lim, A. Migani and K. M. Neyman, *J. Mater. Chem. A*, 2014, **2**, 18329.
- ⁵⁷ J. Divins, I. Angurell, C. Escudero, V. Pérez-Dieste and J. Llorca, *Science*, 2014, **346**, 620.
- ⁵⁸ A. Lebugle, U. Axelsson, R. Nyholm and N. Martensson, *Phys. Scripta*, 1981, **23**, 825.
- ⁵⁹ G. C. Allen, S. J. Harris, J. A. Jutson and J. M. Dyke, *Appl. Surf. Sci.*, 1989, **37**, 111.
- ⁶⁰ V. Matolin, I. Matolinova, M. Vaclavu, I. Khalakhan, M. Vorokhta, R. Fiala, I. Pis, Z. Sofer, J. Poltiero va-Vejpravova, T. Mori, V. Potin, H. Yoshikawa, S. Ueda and K. Kobayashi, *Langmuir*, 2010, **26**, 12824.
- ⁶¹ D. Briggs and M. P. Seah, *Practical Surface Analysis*, 2nd Ed., Vol. 1, Auger and X-ray photoelectron Spectroscopy, Ed. John Wiley & Sons, Chichester, 1990.
- ⁶² S. Tanuma, C. J. Powell and D. R. Penn, *Surf. Interf. Anal.*, 1993, **21**, 165.
- ⁶³ J. J. Yeh, *Atomic Calculation of Photoionization Cross-Sections and Asymmetry Parameters*, Gordon and Breach Science Publishers, Langhorne, PE (USA), 1993.
- ⁶⁴ J. J. Yeh and I. Lindau, *Atomic Data and Nuclear Data Tables*, 1985, **32**, 1.